Letter   Editors' Suggestion

Transition from metal to higher-order topological insulator driven by random flux

Chang-An Li [1,*] Song-Bo Zhang [1,†] Jan Carl Budich,[2,3] and Björn Trauzettel[1,3]
[1]*Institute for Theoretical Physics and Astrophysics, University of Würzburg, 97074 Würzburg, Germany*
[2]*Institute of Theoretical Physics, Technische Universität Dresden, 01062 Dresden, Germany*
[3]*Würzburg-Dresden Cluster of Excellence ct.qmat, Germany*

Random flux is commonly believed to be incapable of driving full metal-insulator transitions in noninteracting systems. Here we show that random flux can after all induce a full metal–band insulator transition in the two-dimensional Su-Schrieffer-Heeger model. Remarkably, we find that the resulting insulator can be an extrinsic higher-order topological insulator with zero-energy corner modes in proper regimes, rather than a conventional Anderson insulator. Employing both level statistics and finite-size scaling analysis, we characterize the metal–band insulator transition and numerically extract its critical exponent as $\nu = 2.48 \pm 0.08$. To reveal the physical mechanism underlying the transition, we present an effective band structure picture based on the random-flux averaged Green's function.

Introduction. Disorder, being present in most physical systems, constitutes a broad field of physics research. As one of its most salient effects, random potential disorder can induce metal–Anderson insulator transitions in various systems [1–5], prominently topological phase transitions [6–9], as recently observed in cold-atom and photonic systems [10,11]. Random flux is another generic type of disorder that has been widely investigated in two-dimensional (2D) electron systems [12–24]. Yet, it is believed that random flux is unable to drive a system with chiral symmetry from metal to Anderson insulator if the Fermi energy locates precisely at zero; instead it localizes all states except the ones at the band center [12,13]. Moreover, the interplay between random flux and topology has barely been explored.

In this work, we discover a random-flux driven metal–band insulator transition. To this end, we add random flux to the 2D Su-Schrieffer-Heeger (SSH) lattice model [Fig. 1(a)], which has attracted broad interest recently [25–27]. In the absence of random flux, this model has been realized in different physical platforms [28–35], and sparked the rapidly developing field of higher-order topological phases [29–55]. Importantly, the existence of a metallic phase in the clean 2D SSH model and its rich topological properties due to nontrivial inner degrees of freedom provide a promising playground for revisiting the issue of random-flux driven transitions in the context of topological band structures.

Remarkably, we find that the spectrum of the system acquires a finite bulk gap in a broad parameter range when exceeding a critical strength of random flux [Figs. 1(c) and 1(d)], thus transforming from a metallic phase to a band insulator. This metal–band insulator transition is confirmed and carefully analyzed by employing energy level statistics and

finite-size scaling theory. The corresponding critical exponent is estimated to be $\nu = 2.48 \pm 0.08$. Interestingly, we find that the band insulator induced by random flux can be an extrinsic higher-order topological insulator (HOTI) by calculating the topological index q_{xy} and identifying the corresponding boundary signatures. Furthermore, with an effective band structure picture based on the flux-averaged Green's function, we show that the metal–band insulator transition can be attributed to the emergence of strongly momentum-dependent flux-induced terms that have a nontrivial matrix structure in the effective Hamiltonian. By contrast, such an interplay of random flux and internal degrees of freedom in the unit cell is absent in the conventional random-flux model.

2D SSH lattice with random flux. As visualized in Fig. 1(a), the 2D SSH lattice model features dimerized hopping amplitudes along both x and y directions [25]. In the absence of disorder, it can be described by the Hamiltonian

$$H_0(\mathbf{k}) = (t_x + t\cos k_x)\tau_1\sigma_0 - t\sin k_x \tau_2\sigma_3$$
$$+ (t_y + t\cos k_y)\tau_1\sigma_1 - t\sin k_y \tau_1\sigma_2, \quad (1)$$

where τ and σ are Pauli matrices for different degrees of freedom within a unit cell; $\mathbf{k} = (k_x, k_y)$ is the 2D wave-vector; t and t_x (t_y) denote the two staggered hopping strengths in the x (y) direction. For simplicity, we put the lattice constant to unity and assume $t > 0$. Note that k_x and k_y are decoupled in Eq. (1). The total Hamiltonian can be recast as the sum of two SSH models along x and y directions, respectively, i.e., $H_0(\mathbf{k}) = H_x(k_x) + H_y(k_y)$. The matrices $\tau_1\sigma_0$ and $\tau_2\sigma_3$ contained in $H_x(k_x)$ anticommute with each other. The same holds for the matrices $\tau_1\sigma_1$ and $\tau_1\sigma_2$ contained in $H_y(k_y)$. However, the two blocks commute with each other, i.e., $[H_x(k_x), H_y(k_y)] = 0$. As a consequence, the four energy bands of Eq. (1) are given by $E_\eta^\pm = \pm[\epsilon_x(k_x) + (-1)^\eta \epsilon_y(k_y)]$ with $\epsilon_\alpha(k_\alpha) = \sqrt{t_\alpha^2 + 2t_\alpha t\cos k_\alpha + t^2}$, $\alpha \in \{x, y\}$, and $\eta \in \{1, 2\}$. When $||t_x| - |t_y|| < 2t$, the system is in a metallic

*changan.li@uni-wuerzburg.de
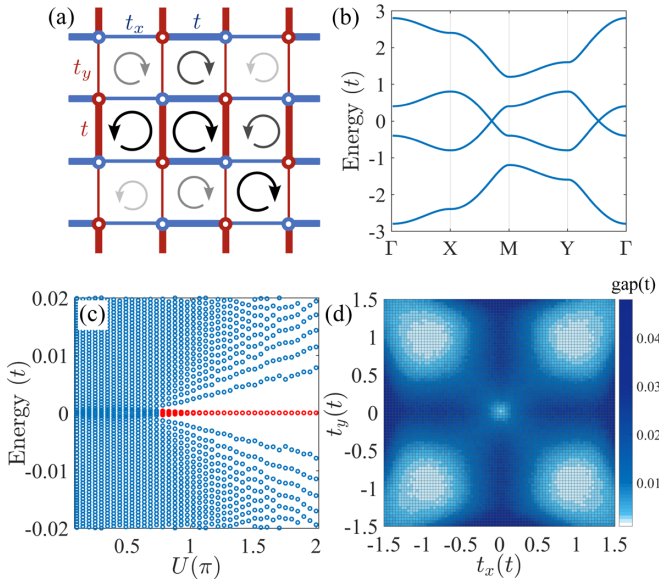†songbo.zhang@physik.uzh.ch

FIG. 1. (a) Schematic of the 2D SSH model with random flux. Blue (red) thick and thin bonds mark dimerized hopping amplitudes in the x (y) direction. The round arrow (with different sizes and opacities) in each plaquette indicates the random flux. (b) Energy spectrum of the model without random flux for $(t_x, t_y) = (0.2t, 0.6t)$. (c) Disorder-averaged spectrum as a function of U for $(t_x, t_y) = (0.2t, 0.6t)$. For large U, the system acquires a bulk gap that protects four zero-energy modes (red). (d) Density plot of the directly disorder-averaged gap as a function of t_x and t_y at $U = 2\pi$. The dimension of the system is $L \equiv L_x = L_y = 30$ with open (periodic) boundaries in (c) [(d)]. Here, 200 random-flux configurations are considered.

phase at low energies [Fig. 1(b)]. The model has C_{2v} group symmetry in general ($t_x \neq t_y$). Moreover, it respects chiral symmetry $\gamma_5 H_0(\mathbf{k}) \gamma_5^{-1} = -H_0(\mathbf{k})$ with the chiral operator $\gamma_5 = \tau_3 \sigma_0$. In the clean case, the constituting 1D blocks along x and y directions are topologically nontrivial when $|t_x| < t$ and $|t_y| < t$, respectively. This property can be identified by symmetry indicators based on the symmetry representations at high-symmetry points in the Brillouin zone that are described in Refs. [56–59]. We note that there may be corner-localized bound states in the bulk continuum, while their stability needs to be protected by C_{4v} symmetry [60,61] which corresponds to $t_x = t_y$ in Eq. (1).

We now add random flux to the model such that each plaquette encloses a flux that has random values drawn from a uniformly distributed interval $[-U/2, U/2]$, as illustrated in Fig. 1(a). Here, U is the strength of random flux within the range of $[0, 2\pi]$, in units of the magnetic flux quantum $\Phi_0 = hc/e$ [62]. The random flux generates random Peierls phases in the hopping matrix elements. Thus, time reversal symmetry is broken. However, chiral symmetry is still preserved and plays a crucial role in the metal-insulator transition as we elaborate below. Note that when each plaquette encloses a π flux uniformly, the system is deformed to the Benalcazar-Bernevig-Hughes (BBH) model [26,27].

Metal–band insulator transition driven by random flux. Next, we demonstrate the existence of random-flux driven metal–band insulator transitions in the 2D SSH model by

employing level statistics [63,64]. In the presence of chiral symmetry, the model falls into the chiral unitary universality class, i.e., AIII in the AZ classification [65]. The insulating and metallic phases can be distinguished by inverse participation ratio (IPR) [66–68] and level spacing ratio (LSR) [53,69]. The IPR is defined by the eigenstates $\phi_n(\mathbf{R}, \zeta)$ of the system as

$$I_n = \sum_{\mathbf{R}} \sum_{\zeta=1}^{4} |\phi_n(\mathbf{R}, \zeta)|^4, \qquad (2)$$

where the sums run over all unit cells labeled by $\mathbf{R}$ and the inner degrees of freedom ζ within a unit cell. The subscript n stands for the nth state with the corresponding eigenenergy E_n listed in ascending order. The LSR is defined in terms of the spectrum as [69]

$$r_n = \frac{\min(s_n, s_{n-1})}{\max(s_n, s_{n-1})}, \qquad (3)$$

where $s_n \equiv E_{n+1} - E_n$ is the difference between two adjacent energy levels. Both the averaged IPR $\langle I \rangle$ and LSR $\langle r \rangle$ take different values in the metallic and insulating limits, thus providing important tools to characterize metal-insulator transitions.

We show below that the level statistics smoothly cross over between the two limits as the random flux drives the system from a metallic to an insulating phase. Due to the presence of chiral symmetry, the eigenenergies of the system come in pairs ($\pm E_n$). For illustration, we take $t_x = 0.2t$ and $t_y = 0.6t$ and consider an energy window containing N_E energy levels around $E = 0$. Figure 2(a) displays $\langle I \rangle$ as a function of U. Clearly, $\langle I \rangle$ increases monotonically from nearly zero in the small U limit to finite values for large U. This indicates that the system transits from a metallic (with vanishing $\langle I \rangle$) to an insulating phase (with finite $\langle I \rangle$). Concomitant with the transformation of $\langle I \rangle$, we also observe that $\langle r \rangle$ decreases smoothly from a universal value 0.6 at small U ($\simeq 0$) to another universal value 0.386 at large U ($\simeq 2\pi$), as shown in Fig. 2(b). For sufficiently large L, the numerical values approach the universal constants in both limits of U. These results agree with those obtained for the uncorrelated Poisson ensemble in the insulating phase ($\langle r \rangle_{\text{ins}} \approx 0.386$) [69] and the unitary ensemble in the metallic phase ($\langle r \rangle_{\text{met}} \approx 0.6$) [70].

To better illustrate the transition, we analyze the probability distribution $P(r)$ of LSR [71]. As shown in Fig. 2(c), $P(r)$ also exhibits universal but different forms in the small and large U regimes [72]. For small U, we find that $P(r)$ can be well described by the distribution function of the Gaussian unitary ensemble (GUE) $P_{\text{GUE}}(r) = \frac{81\sqrt{3}}{2\pi} \frac{(r+r^2)^2}{(1+r+r^2)^4}$ [70]. This finding supports that the system is in a metallic phase. For large U, $P(r)$ instead resembles the uncorrelated Poisson distribution $P_{\text{p}}(r) = \frac{2}{(1+r)^2}$, which again indicates an insulating phase [69]. These results provide direct evidence that the system undergoes a metal-insulator transition by increasing U. This metal-insulator transition is generic for parameters fulfilling $||t_x| - |t_y|| < 2t$, $t_x \neq t$, and $t_x \neq t$ [73]. It is, however, absent for $t_x = t_y = t$, which corresponds to the conventional random-flux model [59]. We note that the band gap opening by random flux [see Fig. 1(c)] may modify the statistical behavior of low energy states close to the band center.
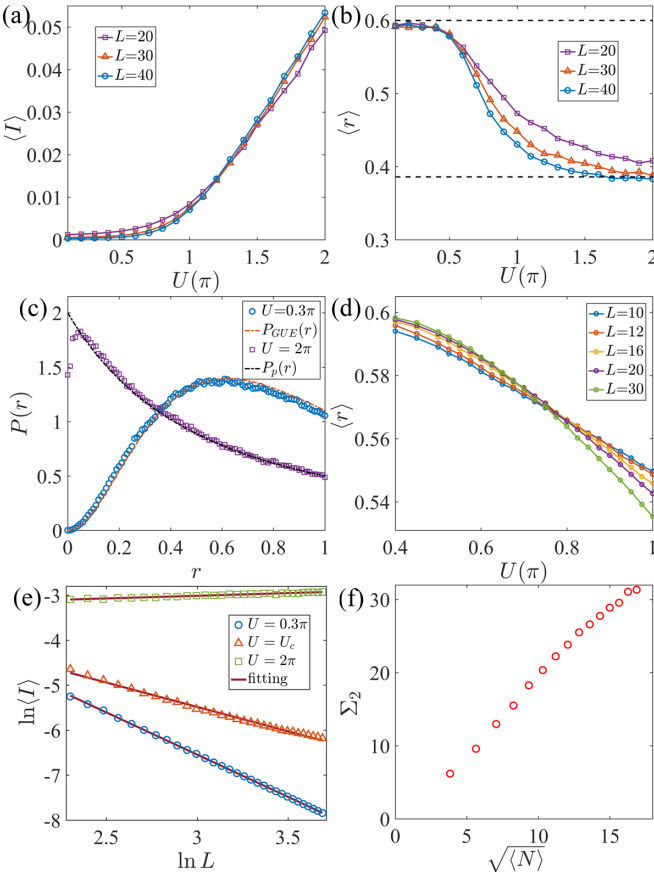
FIG. 2. (a) Averaged IPR $\langle I \rangle$ as a function of U for $L = 20, 30,$ and 40, respectively. (b) Averaged LSR $\langle r \rangle$ as a function of U for $L = 20, 30,$ and 40, respectively. (c) Distribution of LSR $P(r)$ in different limits. (d) Averaged LSR $\langle r \rangle$ near the critical point as a function of U for various L. (e) Scaling behavior of IPR in the metallic (blue) and insulating (green) phases, and at the critical point $U_c \approx 0.75\pi$ (red). (f) Number variance Σ_2 as a function of $\sqrt{\langle N \rangle}$ at the critical point. We consider $N_E = 16$ and 4000 random-flux configurations in (a), (b), (c), and (e). The parameters $t_x = 0.2t$, $t_y = 0.6t$ and periodic boundary conditions are chosen for all plots.

Critical exponent. Critical exponents are keys for characterizing continuous phase transitions. To identify the critical exponent ν and critical random-flux strength U_c, we perform a finite-size scaling analysis of the averaged LSR $\langle r \rangle$ [74–76]. According to the single-parameter scaling theory, $\langle r \rangle$ shows a size-independent value at $U = U_c$. Concentrating around the zero energy, we fix the energy window to capture 10% of the eigenvalues and choose the number of random-flux configurations in such a way that the total eigenvalue number reaches 5×10^7. As shown in Fig. 2(d), $\langle r \rangle$ increases as system size L grows before the transition whereas it decreases as L grows after the transition. The scaling argument near U_c states that $\langle r \rangle$ can be described by a universal function of the form $F(f_1(u)L^{1/\nu}, f_2(u)L^{-y})$ characterized by ν, where $u \equiv (U - U_c)/U_c$, and y is an auxiliary exponent; $f_1(u)L^{1/\nu}$ and $f_2(u)L^{-y}$ stand for relevant and irrelevant length-scale corrections, respectively [76,77]. Close to U_c, we expand $f_\eta(u) = \sum_{j=0}^{m_\eta} a_j^\eta u^j$ with $\eta \in \{1, 2\}$. Thus, ν and U_c can be identified by fitting the Taylor expansion of the function F

near the critical point [76,77]. Thereby, we identify the critical exponent of the random-flux driven metal–band insulator transition as $\nu = 2.48 \pm 0.08$. This critical exponent is close to that of integer quantum Hall transitions with $\nu \approx 2.59$ [78]. In contrast to ν [79], the critical strength U_c depends explicitly on the parameters t_x and t_y. For the parameters considered in Fig. 2(d), we find $U_c \approx 0.75\pi$, in accordance with the gap opening [Fig. 1(c)].

Fractal dimension and spectral rigidity. At the critical point, the wave functions of the system show multifractality due to strong fluctuations [80,81]. The multifractality gives rise to one of the fractal dimensions d_2 defined through the scaling behavior $\langle I \rangle \propto L^{-d_2}$. Figure 2(e) displays $\ln\langle I \rangle$ as a function of $\ln L$ at small, large, and critical values of U, respectively. At the critical point $U = U_c$ (triangles), we can extract $d_2 = 1.085 \pm 0.034$. At $U = 0.3\pi$ (circles) and $U = 2\pi$ (squares), we obtain $d_2 = 1.880 \pm 0.006$ and 0.119 ± 0.008, which are close to the values of an ideal metal (corresponding to $d_2 = 2$) and an insulator (corresponding to $d_2 = 0$), respectively.

The spectral rigidity is also related to the wave-function multifractality. It is defined as the level number variance $\Sigma_2 \equiv \langle N^2 \rangle - \langle N \rangle^2$ in an energy window, where $\langle N \rangle$ is the disorder-averaged number of energy levels within this window. For conventional Anderson transitions, $\Sigma_2 \propto \langle N \rangle$ at the critical point when the energy window is sufficiently large. The ratio $\chi \equiv \Sigma_2/\langle N \rangle$ defines the compressibility of the spectrum. It is conjectured that d_2 is related to χ by the relation $\chi = (2 - d_2)/4$ in 2D [82,83]. However, our scaling law follows instead $\Sigma_2 \propto \sqrt{\langle N \rangle}$ [Fig. 2(f)], resembling the complex Ginibre ensemble [84]. This behavior may be due to the fact that the random flux gives a complex matrix ensemble. Thus, χ goes to zero in the large N limit, and the aforementioned conjecture fails in our system.

Effective band structure picture for the metal–band insulator transition. To reveal the underlying mechanism, we average the Green's function over many random-flux configurations, so as to effectively restore lattice translation invariance and derive the self-energy $\Sigma(\mathbf{k})$ due to the random flux [59,85]. We find that $\Sigma(\mathbf{k})$ not only modifies the coefficient functions of the matrices in the original Hamiltonian [cf. Eq. (1)] but also introduces additional terms associated with new matrices $\tau_1\sigma_3$ and $\tau_2\sigma_0$ (that also appear in the BBH model). This feature can be understood in terms of higher-order scattering processes induced by random flux. It is intimately related to the interplay between the internal degrees of freedom of the model and the random flux that couples directly to momentum in the system. Consequently, $\Sigma(\mathbf{k})$ decisively depends on momentum. These observations indicate that the effective Hamiltonian $H_{\mathrm{eff}}(\mathbf{k}) \equiv H_0(\mathbf{k}) + \Sigma(\mathbf{k})$ for the system with random flux can be regarded as a mixture of the 2D SSH and BBH models. Remarkably, a band gap for strong U can be directly revealed by the effective band structure of $H_{\mathrm{eff}}(\mathbf{k})$ [59]. The critical value U_c of random-flux strength obtained here is consistent with the numerical result in Fig. 1(c). In this sense, the random flux generates a band insulator by opening an effective gap in the bulk after the transition.

Extrinsic HOTI induced by random flux. Now, we show that in the parameter regime $|t_x| < t$ and $|t_y| < t$ the band insulator
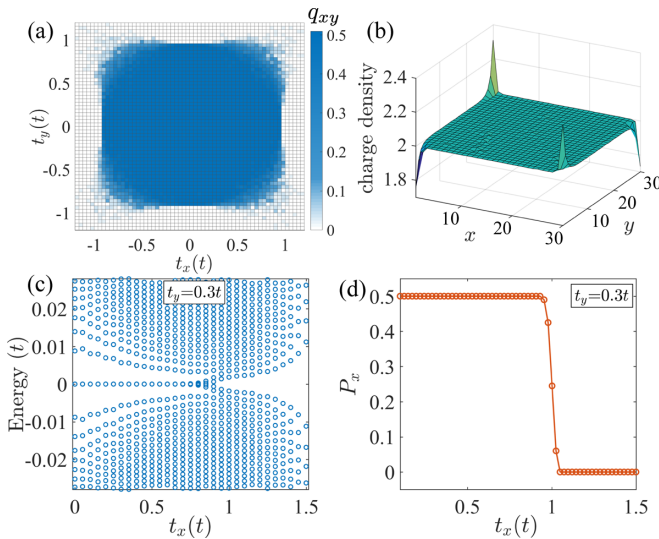
FIG. 3. (a) Phase diagram of q_{xy} against t_x and t_y. The dimension of the system is $L = 30$ with 30 random-flux configurations. (b) Electron charge density in the extrinsic HOTI phase at half filling. (c) Disorder-averaged energy spectrum as a function of t_x for $t_y = 0.3t$ under open boundary conditions. (d) Disorder-averaged edge polarization P_x as a function of t_x for $t_y = 0.3t$. $U = 2\pi$ for all plots.

induced by random flux can be an extrinsic HOTI [40,41]. For concreteness, we consider $U = 2\pi$. In this case, the system is an insulator with a finite energy gap, unless $|t_x| = |t_y| = t$; cf. Fig. 1(d) [86]. Note that the disorder-averaged flux on each plaquette is zero. The defined electric quadrupole moment q_{xy} can provide a topological index to characterize the extrinsic HOTI [26,27,87–89]. In the phase diagram shown in Fig. 3(a), which is similar to that of BBH model, we observe a nontrivial region (blue) with a half quantized $q_{xy} = 1/2$. In the outer region (white), the system is a trivial insulator with $q_{xy} = 0$. This implies that the random-flux driven higher-order topological phases can be continuously connected to that of the BBH model. The quantization of q_{xy} is protected by chiral symmetry [51]. Accordingly, a nontrivial q_{xy} indicates the emergence of zero-energy modes at the corners of the system. This is confirmed numerically in Figs. 1(c) and 3(c) where four zero-energy modes clearly emerge in the nontrivial phase whereas they disappear in the trivial phase. Furthermore, we calculate the local charge density at half filling [Fig. 3(b)]. Summing the charge density over each quadrant including a single corner, we find that the total charge takes fractional values $\pm 1/2$ as long as L is large enough. These fractional corner charges provide another hallmark of the HOTI.

For a fixed strong U, the system transits between an extrinsic HOTI and a trivial insulator by changing t_x or t_y. Due to its

extrinsic nature, the topological phase transitions take place at the boundaries instead of the bulk of the system. To elucidate this phase transition, we calculate the effective Hamiltonian H_{edge} for edges in the presence of random flux via a recursive Green's function method [90,91]. We see the edge spectrum close and reopen around phase boundary. Alternatively, the transition can also be shown from the edge polarization of H_{edge} [27,92]. For illustration, we consider the edge along x direction and present the disorder-averaged polarization P_x as a function of t_x in Fig. 3(d). Near $t_x = t$, P_x changes suddenly from 1/2 to 0, indicating a topological phase transition. The results for edges along y direction can be obtained similarly. We note that the system is nontrivial only if both edge Hamiltonians along x and y directions are nontrivial.

Discussion and conclusions. Note that the metal–band insulator transition driven by random flux is found to also occur in the topologically trivial regime [59], which indicates its generality. Clearly, the random flux with zero mean is different from the case with a uniform flux, where the Hofstadter butterfly emerges [93–95]. In the limit of $t_x = t_y = t$, our system reduces to the conventional random-flux model. In this limit, we recover the well established result that the bulk states at the band center stay delocalized and no metal-insulator transition occurs [59]. We emphasize that the random-flux driven metal–band insulator transition is distinctively different from related work in interacting systems [23,24] where the competition between (random) flux and electron-electron interaction is responsible for an interaction driven phase transition.

The 2D SSH model can be realized in different platforms such as metamaterials [30–34] and microwave and electric circuits [29,35,96,97]. In particular, the manipulation of effective magnetic fluxes has become experimentally accessible in sonic crystals and circuit simulators [98,99]. Therefore, these materials may provide us with promising platforms to test our predictions by taking advantage of their high controllability.

In conclusion, based on the 2D SSH model we have revealed an example of a metal–band insulator transition that is solely driven by random flux. We have analyzed this metal–band insulator transition by level statistics and finite-size scaling theory, and found the critical exponent as $\nu = 2.48 \pm 0.08$. It is shown that the emergent insulator can be an extrinsic HOTI by presenting its phase diagram and characteristic boundary signatures. We have further proposed an effective band structure picture to understand the metal–band insulator transition driven by random flux.

[1] P. W. Anderson, Absence of diffusion in certain random lattices, Phys. Rev. **109**, 1492 (1958).

[2] F. Evers and A. D. Mirlin, Anderson transitions, Rev. Mod. Phys. **80**, 1355 (2008).

[3] L. Sanchez-Palencia and M. Lewenstein, Disordered quantum gases under control, Nat. Phys. **6**, 87 (2010).

[4] T. Schwartz, G. Bartal, S. Fishman, and M. Segev, Transport and Anderson localization in disordered two-

dimensional photonic lattices, Nature (London) **446**, 52 (2007).

[5] J. Chabé, G. Lemarié, B. Grémaud, D. Delande, P. Szriftgiser, and J. C. Garreau, Experimental Observation of the Anderson Metal-Insulator Transition with Atomic Matter Waves, Phys. Rev. Lett. **101**, 255702 (2008).

[6] J. Li, R.-L. Chu, J. K. Jain, and S.-Q. Shen, Topological Anderson Insulator, Phys. Rev. Lett. **102**, 136806 (2009).

[7] C. W. Groth, M. Wimmer, A. R. Akhmerov, J. Tworzydło, and C. W. J. Beenakker, Theory of the Topological Anderson Insulator, Phys. Rev. Lett. **103**, 196805 (2009).

[8] H. Jiang, L. Wang, Q.-F. Sun, and X. C. Xie, Numerical study of the topological Anderson insulator in HgTe/CdTe quantum wells, Phys. Rev. B **80**, 165316 (2009).

[9] H.-M. Guo, G. Rosenberg, G. Refael, and M. Franz, Topological Anderson Insulator in Three Dimensions, Phys. Rev. Lett. **105**, 216601 (2010).

[10] E. J. Meier, F. A. An, A. Dauphin, M. Maffei, P. Massignan, T. L. Hughes, and B. Gadway, Observation of the topological Anderson insulator in disordered atomic wires, Science **362**, 929 (2018).

[11] S. Stützer, Y. Plotnik, Y. Lumer, P. Titum, N. H. Lindner, M. Segev, M. C. Rechtsman, and A. Szameit, Photonic topological Anderson insulators, Nature (London) **560**, 461 (2018).

[12] V. Z. Cerovski, Critical exponent of the random flux model on an infinite two-dimensional square lattice and anomalous critical states, Phys. Rev. B **64**, 161101(R) (2001).

[13] A. Furusaki, Anderson Localization due to a Random Magnetic Field in Two Dimensions, Phys. Rev. Lett. **82**, 604 (1999).

[14] A. G. Aronov, A. D. Mirlin, and P. Wölfle, Localization of charged quantum particles in a static random magnetic field, Phys. Rev. B **49**, 16609 (1994).

[15] D. Taras-Semchuk and K. B. Efetov, Antilocalization in a 2D Electron Gas in a Random Magnetic Field, Phys. Rev. Lett. **85**, 1060 (2000).

[16] D. N. Sheng and Z. Y. Weng, Delocalization of Electrons in a Random Magnetic Field, Phys. Rev. Lett. **75**, 2388 (1995).

[17] D. Z. Liu, X. C. Xie, S. Das Sarma, and S. C. Zhang, Electron localization in a two-dimensional system with random magnetic flux, Phys. Rev. B **52**, 5858 (1995).

[18] S.-C. Zhang and D. P. Arovas, Effective Field Theory of Electron Motion in the Presence of Random Magnetic Flux, Phys. Rev. Lett. **72**, 1886 (1994).

[19] R. Gade, Anderson localization for sublattice models, Nucl. Phys. B **398**, 499 (1993).

[20] T. Sugiyama and N. Nagaosa, Localization in a Random Magnetic Field in 2D, Phys. Rev. Lett. **70**, 1980 (1993).

[21] Y. Avishai, Y. Hatsugai, and M. Kohmoto, Localization problem of a two-dimensional lattice in a random magnetic field, Phys. Rev. B **47**, 9561 (1993).

[22] P. A. Lee and D. S. Fisher, Anderson Localization in Two Dimensions, Phys. Rev. Lett. **47**, 882 (1981).

[23] J. An, C. D. Gong, and H. Q. Lin, Theory of the magnetic-field-induced metal-insulator transition, Phys. Rev. B **63**, 174434 (2001).

[24] M. S. Foster and A. W. W. Ludwig, Metal-insulator transition from combined disorder and interaction effects in Hubbard-like electronic lattice models with random hopping, Phys. Rev. B **77**, 165108 (2008).

[25] F. Liu and K. Wakabayashi, Novel Topological Phase with a Zero Berry Curvature, Phys. Rev. Lett. **118**, 076803 (2017).

[26] W. A. Benalcazar, B. A. Bernevig, and T. L. Hughes, Quantized electric multipole insulators, Science **357**, 61 (2017).

[27] W. A. Benalcazar, B. A. Bernevig, and T. L. Hughes, Electric multipole moments, topological multipole moment pumping, and chiral hinge states in crystalline insulators, Phys. Rev. B **96**, 245115 (2017).

[28] F. Schindler, Z. Wang, M. G. Vergniory, A. M. Cook, A. Murani, S. Sengupta *et al.*, Higher-order topology in bismuth, Nat. Phys. **14**, 918 (2018).

[29] S. Imhof, C. Berger, F. Bayer, J. Brehm, L. W. Molenkamp, T. Kiessling *et al.*, Topolectrical-circuit realization of topological corner modes, Nat. Phys. **14**, 925 (2018).

[30] M. Serra-Garcia, V. Peri, R. Süsstrunk, O. R. Bilal, T. Larsen, L. G. Villanueva, and S. D. Huber, Observation of a phononic quadrupole topological insulator, Nature (London) **555**, 342 (2018).

[31] B.-Y. Xie, G.-X. Su, H.-F. Wang, H. Su, X.-P. Shen, P. Zhan, M.-H. Lu, Z.-L. Wang, and Y.-F. Chen, Visualization of Higher-Order Topological Insulating Phases in Two-Dimensional Dielectric Photonic Crystals, Phys. Rev. Lett. **122**, 233903 (2019).

[32] Y. Qi, C. Qiu, M. Xiao, H. He, M. Ke, and Z. Liu, Acoustic Realization of Quadrupole Topological Insulators, Phys. Rev. Lett. **124**, 206601 (2020).

[33] X. Ni, M. Weiner, A. Alù, and A. B. Khanikaev, Observation of higher-order topological acoustic states protected by generalized chiral symmetry, Nat. Mater. **18**, 113 (2019).

[34] X.-D. Chen, W.-M. Deng, F.-L. Shi, F.-L. Zhao, M. Chen, and J.-W. Dong, Direct Observation of Corner States in Second-Order Topological Photonic Crystal Slabs, Phys. Rev. Lett. **122**, 233902 (2019).

[35] C. W. Peterson, W. A. Benalcazar, T. L. Hughes, and G. Bahl, A quantized microwave quadrupole insulator with topologically protected corner states, Nature (London) **555**, 346 (2018).

[36] J. Langbehn, Y. Peng, L. Trifunovic, F. von Oppen, and P. W. Brouwer, Reflection-Symmetric Second-Order Topological Insulators and Superconductors, Phys. Rev. Lett. **119**, 246401 (2017).

[37] Z. Song, Z. Fang, and C. Fang, $(d-2)$-Dimensional Edge States of Rotation Symmetry Protected Topological States, Phys. Rev. Lett. **119**, 246402 (2017).

[38] F. Schindler, A. M. Cook, M. G. Vergniory, Z. Wang, S. S. P. Parkin, B. A. Bernevig, and T. Neupert, Higher-order topological insulators, Sci. Adv. **4**, eaat0346 (2018).

[39] M. Ezawa, Higher-Order Topological Insulators and Semimetals on the Breathing Kagome and Pyrochlore Lattices, Phys. Rev. Lett. **120**, 026801 (2018).

[40] M. Geier, L. Trifunovic, M. Hoskam, and P. W. Brouwer, Second-order topological insulators and superconductors with an order-two crystalline symmetry, Phys. Rev. B **97**, 205135 (2018).

[41] L. Trifunovic and P. W. Brouwer, Higher-Order Bulk-Boundary Correspondence for Topological Crystalline Phases, Phys. Rev. X **9**, 011012 (2019).

[42] F. Liu, H.-Y. Deng, and K. Wakabayashi, Helical Topological Edge States in a Quadrupole Phase, Phys. Rev. Lett. **122**, 086804 (2019).

[43] X.-W. Luo and C. Zhang, Higher-Order Topological Corner States Induced by Gain and Loss, Phys. Rev. Lett. **123**, 073601 (2019).

[44] S. A. A. Ghorashi, T. Li, and T. L. Hughes, Higher-Order Weyl Semimetals, Phys. Rev. Lett. **125**, 266804 (2020).

[45] H.-X. Wang, Z.-K. Lin, B. Jiang, G.-Y. Guo, and J.-H. Jiang, Higher-Order Weyl Semimetals, Phys. Rev. Lett. **125**, 146401 (2020).

[46] K. Kudo, T. Yoshida, and Y. Hatsugai, Higher-Order Topological Mott Insulators, Phys. Rev. Lett. **123**, 196402 (2019).

[47] Y. Volpez, D. Loss, and J. Klinovaja, Second-Order Topological Superconductivity in π-Junction Rashba Layers, Phys. Rev. Lett. **122**, 126402 (2019).

[48] Z. Wang, B. J. Wieder, J. Li, B. Yan, and B. A. Bernevig, Higher-Order Topology, Monopole Nodal Lines, and the Origin of Large Fermi Arcs in Transition Metal Dichalcogenides $X\text{Te}_2$ ($X =$ Mo, W), Phys. Rev. Lett. **123**, 186401 (2019).

[49] Z. Yan, F. Song, and Z. Wang, Majorana Corner Modes in a High-Temperature Platform, Phys. Rev. Lett. **121**, 096803 (2018).

[50] R.-X. Zhang, F. Wu, and S. Das Sarma, Möbius Insulator and Higher-Order Topology in $\text{MnBi}_{2n}\text{Te}_{3n+1}$, Phys. Rev. Lett. **124**, 136407 (2020).

[51] C.-A. Li, B. Fu, Z.-A. Hu, J. Li, and S.-Q. Shen, Topological Phase Transitions in Disordered Electric Quadrupole Insulators, Phys. Rev. Lett. **125**, 166801 (2020).

[52] R. Chen, C.-Z. Chen, J.-H. Gao, B. Zhou, and D.-H. Xu, Higher-Order Topological Insulators in Quasicrystals, Phys. Rev. Lett. **124**, 036803 (2020).

[53] Y.-B. Yang, K. Li, L.-M. Duan, and Y. Xu, Higher-order topological Anderson insulators, Phys. Rev. B **103**, 085408 (2021).

[54] S.-B. Zhang, W. B. Rui, A. Calzona, S.-J. Choi, A. P. Schnyder, and B. Trauzettel, Topological and holonomic quantum computation based on second-order topological superconductors, Phys. Rev. Research **2**, 043025 (2020).

[55] T. Li, M. Geier, J. Ingham, and H. D. Scammell, Higher-order topological superconductivity from repulsive interactions in kagome and honeycomb systems, 2D Mater. **9**, 015031 (2022).

[56] W. A. Benalcazar, T. Li, and T. L. Hughes, Quantization of fractional corner charge in C_n-symmetric higher-order topological crystalline insulators, Phys. Rev. B **99**, 245151 (2019).

[57] J. Kruthoff, J. de Boer, J. van Wezel, C. L. Kane, and R. J. Slager, Topological Classification of Crystalline Insulators through Band Structure Combinatorics, Phys. Rev. X **7**, 041069 (2017).

[58] H. C. Po, A. Vishwanath, and H. Watanabe, Symmetry-based indicators of band topology in the 230 space groups, Nat. Commun. **8**, 50 (2017).

[59] See Supplemental Material at http://link.aps.org/supplemental/10.1103/PhysRevB.106.L081410 for more details on the properties of 2D SSH model and the effective band structure picture for the metal-band insulator transition, including Refs. [13,56,60].

[60] W. A. Benalcazar and A. Cerjan, Bound states in the continuum of higher-order topological insulators, Phys. Rev. B **101**, 161116(R) (2020).

[61] A. Cerjan, M. Jürgensen, W. A. Benalcazar, S. Mukherjee, and M. C. Rechtsman, Observation of a Higher-Order Topological Bound State in the Continuum, Phys. Rev. Lett. **125**, 213901 (2020).

[62] On an experimental note, the feasibility of manipulating gauge fluxes in these systems was recently demonstrated [98].

[63] E. P. Wigner, On a class of analytic functions from the quantum theory of collisions, Ann. Math. **53**, 36 (1951).

[64] F. J. Dyson, Statistical theory of the energy levels of complex systems. I, J. Math. Phys. **3**, 140 (1962).

[65] A. Altland and M. R. Zirnbauer, Nonstandard symmetry classes in mesoscopic normal-superconducting hybrid structures, Phys. Rev. B **55**, 1142 (1997).

[66] X. Li, X. Li, and S. Das Sarma, Mobility edges in one-dimensional bichromatic incommensurate potentials, Phys. Rev. B **96**, 085119 (2017).

[67] S. Roy, T. Mishra, B. Tanatar, and S. Basu, Reentrant Localization Transition in a Quasiperiodic Chain, Phys. Rev. Lett. **126**, 106803 (2021).

[68] A. Padhan, M. K. Giri, S. Mondal, and T. Mishra, Emergence of multiple localization transitions in a one-dimensional quasiperiodic lattice, Phys. Rev. B **105**, L220201 (2022).

[69] V. Oganesyan and D. A. Huse, Localization of interacting fermions at high temperature, Phys. Rev. B **75**, 155111 (2007).

[70] Y. Y. Atas, E. Bogomolny, O. Giraud, and G. Roux, Distribution of the Ratio of Consecutive Level Spacings in Random Matrix Ensembles, Phys. Rev. Lett. **110**, 084101 (2013).

[71] Note that in the thermodynamic limit, the discrete LSR r_n becomes a continuous variable $r \in [0, 1]$.

[72] At the critical point, the distribution $P_c(r)$ is different from these two limits (see Supplemental Material [59]).

[73] Here, we consider the case with $|t_x| < t$ and $|t_y| < t$ for concreteness. We provide the calculations for other parameter regimes, for instance with $|t_x| > t$ and $|t_y| > t$ and for the random-flux model limit with $t_x = t_y = t$ in the Supplemental Material [59].

[74] C. R. Laumann, A. Pal, and A. Scardicchio, Many-Body Mobility Edge in a Mean-Field Quantum Spin Glass, Phys. Rev. Lett. **113**, 200405 (2014).

[75] D. J. Luitz, N. Laflorencie, and F. Alet, Many-body localization edge in the random-field Heisenberg chain, Phys. Rev. B **91**, 081103(R) (2015).

[76] X. Luo, T. Ohtsuki, and R. Shindou, Universality Classes of the Anderson Transitions Driven by Non-Hermitian Disorder, Phys. Rev. Lett. **126**, 090402 (2021).

[77] K. Slevin and T. Ohtsuki, Critical exponent for the Anderson transition in the three-dimensional orthogonal universality class, New J. Phys. **16**, 015012 (2014).

[78] K. Slevin and T. Ohtsuki, Critical exponent for the quantum Hall transition, Phys. Rev. B **80**, 041304(R) (2009).

[79] According to the general theory of critical phenomena, ν is universal and determined solely by the universality class and the dimension of the system.

[80] F. Evers and A. D. Mirlin, Fluctuations of the Inverse Participation Ratio at the Anderson Transition, Phys. Rev. Lett. **84**, 3690 (2000).

[81] A. D. Mirlin and F. Evers, Multifractality and critical fluctuations at the Anderson transition, Phys. Rev. B **62**, 7920 (2000).

[82] J. T. Chalker, V. E. Kravtsov, and I. V. Lerner, Spectral rigidity and eigenfunction correlations at the Anderson transition, J. Exp. Theor. Phys. **64**, 386 (1996).

[83] J. T. Chalker, I. V. Lerner, and R. A. Smith, Random Walks through the Ensemble: Linking Spectral Statistics with Wave-

Function Correlations in Disordered Metals, Phys. Rev. Lett. **77**, 554 (1996).

[84] J. Ginibre, Statistical ensembles of complex, quaternion, and real matrices, J. Math. Phys. **6**, 440 (1965).

[85] Note that translational symmetry in the system can be restored by such an average. Periodic boundary conditions are imposed in the calculation.

[86] We provide the calculation and analysis for other values of U in the Supplemental Material [59].

[87] B. Kang, K. Shiozaki, and G. Y. Cho, Many-body order parameters for multipoles in solids, Phys. Rev. B **100**, 245134 (2019).

[88] W. A. Wheeler, L. K. Wagner, and T. L. Hughes, Many-body electric multipole operators in extended systems, Phys. Rev. B **100**, 245135 (2019).

[89] B. Roy, Antiunitary symmetry protected higher-order topological phases, Phys. Rev. Research **1**, 032048(R) (2019).

[90] Y. Peng, Y. Bao, and F. von Oppen, Boundary green functions of topological insulators and superconductors, Phys. Rev. B **95**, 235143 (2017).

[91] Based on the layered lattice structure, the Green's function at the nth layer can be expressed as $G_n = (E - H_n - V_{n-1,n}G_{n-1}V_{n-1,n}^\dagger)^{-1}$, where H_n is the Hamiltonian for the nth layer and $V_{n-1,n}$ is the hoping between the $(n-1)$th layer and nth layer. After the iteration process, the edge Hamiltonian can be obtained as $H_{\text{edge}} = -G_{\mathcal{N}}(E=0)^{-1}$, where $\mathcal{N}$ labels the edge layer.

[92] R. Resta, Quantum-Mechanical Position Operator in Extended Systems, Phys. Rev. Lett. **80**, 1800 (1998).

[93] Y. Otaki and T. Fukui, Higher-order topological insulators in a magnetic field, Phys. Rev. B **100**, 245108 (2019).

[94] Z.-W. Zuo, W. A. Benalcazar, and C.-X. Liu, Topological phases of the dimerized hofstadter butterfly, J. Phys. D: Appl. Phys. **54**, 414004 (2021).

[95] D. R. Hofstadter, Energy levels and wave functions of bloch electrons in rational and irrational magnetic fields, Phys. Rev. B **14**, 2239 (1976).

[96] J. Dong, V. Juričić, and B. Roy, Topolectric circuits: Theory and construction, Phys. Rev. Research **3**, 023056 (2021).

[97] W. Zhang, D. Zou, Q. Pei, W. He, J. Bao, H. J. Sun, and X. Zhang, Experimental Observation of Higher-Order Topological Anderson Insulators, Phys. Rev. Lett. **126**, 146802 (2021).

[98] Z.-K. Lin, Y. Wu, B. Jiang, Y. Liu, S.-Q. Wu, F. Li, and J.-H. Jiang, Topological Wannier cycles induced by sub-unit-cell artificial gauge flux in a sonic crystal, Nat. Mater. **21**, 430 (2022).

[99] S. Li, X.-X. Yan, J.-H. Gao, and Y. Hu, Circuit quantum electrodynamics simulator of the two-dimensional Su-Schrieffer-Heeger model: Higher-order topological phase transition induced by a continuously varying magnetic field, Opt. Express **30**, 17054 (2022).